A novel multi-step multi-exposure PTV algorithm with adaptive time separation

E. Saredi[1]*, A. Sciacchitano[1] and F. Scarano[1]
1: Faculty of Aerospace Engineering, Delft University of Technology, Delft, The Netherlands
* Corresponding author: e.saredi@tudelft.nl

Keywords: PIV, double-exposure imaging, PTV algorithm, Dynamic Velocity Range

ABSTRACT

This work proposes a new multi-step measurement algorithm for PTV to cope with high flow velocities that do not allow time-resolved measurements. The proposed methodology relies on an iterative process, whereby a double-frame single-pulse image acquisition is followed by a multi-exposure acquisition. The novelty of the approach lies on the adaptive selection of the time separation used in the second acquisition to maximise the measurement dynamic velocity range and minimise the occurrence of overlapping particle images. The adaptive selection is performed based on the velocity field obtained by the first double-frame single-pulse acquisition and aims to obtain a rather uniform particle displacement across the measurement volume. The proposed methodology is demonstrated based on flow measurements in the near-wake of a truncated cylinder at Re=33,000. The results obtained by the presented method are then compared to those retrieved via the state-of-the-art PTV algorithm Shake-The-Box, a double-frame single-exposure strategy and a standard double-frame double-exposure strategy with a fixed pulse separation time. The increment of the particle displacement in the regions characterized by low velocity leads to a reduction of the relative uncertainty on the evaluated velocity and a consequent increase of the achievable dynamic velocity range. Among the double-frame strategies, requirement to allow PTV measurement at relatively high speed, the proposed methodology achieves the lowest error with respect to the reference, given by STB measurement in this case.

1. Introduction

Particle Tracking Velocimetry (PIV) and Particle Tracking Velocimetry (PTV) are nowadays well-establish measurement techniques used both in academic and industrial environments. Between the two methodologies, PIV is often the standard choice due to its robustness at high seeding concentrations (Kähler et al., 2016). The advent of the Shake-The-Box algorithm (STB, Schanz et al., 2016) has allowed PTV to cope with image densities of the same order as the ones encountered in conventional Tomographic PIV experiments (Scarano, 2012). Developed for the analysis of Time-Resolved (TR) recordings, the key point behind the STB algorithm is the exploitation of the time coherency of the particle's motion to increase the robustness of the particle pairing. Nevertheless, several problems of interest both in academia and in industry involve the presence of flow velocities exceeding 50 m/s, for which time-resolved measurements are not feasible with state-of-the-art hardware. At these velocities, the direct application of methodologies that require

TR recordings is not possible due to the current limitations in terms of maximum recording frequency (Novara et al., 2016). A possible solution to overcome this limitation is the adoption of measurements based on dual-frame image recording (e.g. by frame-straddling), with a time separation Δt of the order of microseconds. It is known, however, that dual-frame recordings suffer from a poor dynamic velocity range (DVR, Adrian 1997) when compared to time-resolved measurements (Lynch and Scarano 2013). To enhance the DVR when time-resolved measurements are not possible, Saredi et al. (2020) presented a methodology based on a multi-step approach. Firstly, the velocity field obtained by a double-frame single-pulse measurement with a low Δt, featuring high robustness and low precision, was decomposed via Reynolds decomposition. The time-averaged velocity was then employed to increase the robustness of the pairing performed on a second acquisition done with a higher Δt. The authors showed that the increased time separation of the second image acquisition leads to an increased DVR. However, the lack of time resolution caused by the use of only two exposures limits the accuracy of the measured velocity, and prevents the determination of the particle acceleration, needed to calculate the pressure field (van Oudheusden, 2013). Furthermore, because the velocity field is retrieved from double-frame single-pulse recordings, truncation errors increase with increasing time separation Δt (Boillot and Prasad, 1996).

Another possible approach for coping with high-speed flows relies on the use of multi-exposure recordings, which allow increased measurement accuracy due to tracking particles at multiple time instants, as well as the determination of the particle's accelerations and in turn the pressure field. Two versions of the STB algorithm adopting this strategy have been developed: multi-pulse STB (Novara et al., 2016) and four-pulse Shake-The-Box (Sellappan et al., 2020). The difference between the two presented methodologies lies in the adopted timing strategy to obtain the four particle positions across the two frames, as discussed in the next section. The application of these methodologies has been presented copying with velocities ranging from 35.5 m/s to 290 m/s by Novara et al. (2019) and Godbersen et al. (2019), respectively. However, both the mentioned methodologies make use of fixed time separations among the pulses, thus leading to increased measurement accuracy only locally and not in the entire flow field. Additionally, they suffer from the presence of overlapping particle images in regions of low flow velocities, leading to erroneous particle reconstructions and velocity measurements. Furthermore, no theoretical analysis on the achievable DVR has been presented in the literature, leaving the question of the optimal selection of the time separation among pulses unanswered. The current paper aims at solving the limitations of current multi-pulse PTV approaches by proposing a multi-step multi-exposure algorithm with adaptive time separation. The approach, based on a learning paradigm similar to

the one applied in Saredi et al. (2020), guarantees that the measurement accuracy is maximised in the entire flow domain, and that no overlapping particle images are present even in regions of low flow velocities. Additionally, a theoretical framework is developed for the evaluation of the maximum DVR achievable with the different PTV strategies.
In order to prove the effectiveness of the proposed methodology, an experimental dataset concerning the flow around a truncated cylinder at Re=330,000 is considered. The state-of-the-art methodology Shake-The-Box is used to produce the ground truth that is taken as a reference.

2. Achievable DVR of PTV approaches

Let us firstly consider a situation in which no a-priori information of the flow is available and double-frame single-exposure images are acquired, with a particle distribution characterized by a mean inter-particle distance λ in physical space. Commonly, the accuracy of a PIV measurement is evaluated via the Dynamic Velocity Range (DVR), defined as the ratio between the maximum and the minimum resolvable velocities (viz. displacements) (Adrian, 1997):

$$\mathrm{DVR} = \frac{|\mathbf{\Delta X_{max}}|}{\sigma_{\Delta \mathrm{X}}} = \frac{\Delta t\, V_{max}}{\sigma_{\Delta \mathrm{X}}} \qquad (1)$$

The maximum achievable DVR can be increased by either decreasing the uncertainty $\sigma_{\Delta \mathrm{X}}$ of the displacement measurement or increasing the time separation Δt between laser pulses and in turn the particle image displacement.
While the former is dependent on the experimental setup (hardware used, cameras configuration in 3D PIV/LPT) and on the image processing algorithm, the latter is an experimental parameter that can be set to the desired value.
The value of $\sigma_{\Delta \mathrm{X}}$ varies according to the acquisition strategy adopted, however is always function of the particle position uncertainty ε_x. Following the definition given in Adrian (1997), the rms error of the particle position ε_x is proportional to the particle image diameter through the formula $\varepsilon_x = c_\tau\, d_\tau$, where d_τ is the particle particle diameter and c_τ is a constant varying from 1% to 20%, depending on the ability of the system to determine the particle displacement (Adrian and Westerweel, 2011). As stated in Schneiders et al. (2018), the uncertainty of the particle displacement for a double-pulse single-exposure strategy can be then calculated from the superimposition of the variances of the particle position estimation:

$$\sigma_{\Delta \mathrm{X}} = \sqrt{2}\, \varepsilon_x \qquad (2)$$

From this, it follows that the achievable DVR for a double-frame single-exposure acquisition (labelled as DF hereafter) reads as:

$$\mathrm{DVR_{DF}} = \frac{|\mathbf{\Delta X_{max}}|}{\sqrt{2} c_\tau \, d_\tau} \qquad (3)$$

Eq. (1) suggests that extending the particle separation time between two subsequent illuminations is always beneficial for the increase of the achievable DVR. For LPT measurement, this result is correct only if the streamline curvature is negligible (no truncation errors) and the possibility of false particle pairing is not considered, neglecting the presence of other particles in the research volume. As shown in Saredi et al. (2020), the mean particle distance λ plays an important role in determining the maximum allowed particle displacement. However, in the discussion of this paper, the mean inter-particle distance is assumed to be much larger than the particle image displacement. Hence, errors due to false particle pairings are neglected and will be analised in future works.

The use of multiple positions of the same particle has been proven effective in increasing the precision of the velocity determination (Cierpka et al., 2013; Lynch and Scarano, 2013; Schanz et al., 2016; amongst others). This can be achieved by acquiring time-resolved data or multi-exposed images. In order to define the achievable DVR in this situation, let us consider a case where the same particle is imaged k times, each with a time separation of Δt, by using one of the two mentioned approaches. The obtained discrete particle positions can be used to build a track, which can be regularized through a polynomial regression, as shown in Fig. 1.

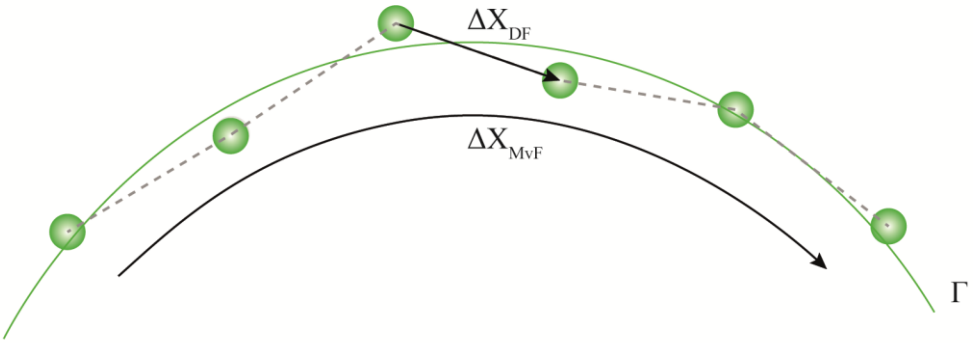

Fig. 1 Schematic representation of particle track evaluated at a discrete number of positions. While the grey line represents the displacement evaluated with a double-pulse single exposure analysis, the green line shows the streamline obtained through a second-order polynomial regression.

The advantages of using multiple discrete particle positions to evaluate the particle velocity arise from two main factors: the total evaluated displacement increases and the effect of random errors on the particle position determination is reduced. For k successive particle image recordings, the displacement increases by factor k with respect to the dual-pulse analysis, whereas the positional uncertainty decreases by $\frac{c_\alpha}{\sqrt{k}}$ (Lynch and Scarano, 2013), with c_α being a coefficient dependent upon

the track regularization technique used. Combining these two effects, the achievable DVR for k recordings of the particles positions is:

$$\mathrm{DVR_{ME}} = \frac{k\sqrt{k}|\mathbf{\Delta X_{max}}|}{c_\alpha\, c_\tau\, d_\tau} \qquad (4)$$

where the ME subscripts stands for multi-exposure. Comparing Eq. (3) and Eq. (4), it is possible to evaluate the DVR gain G_{DVR} when multiple exposures of the same particle are considered:

$$G_{\mathrm{DVR}} = \frac{\mathrm{DVR_{ME}}}{\mathrm{DVR_{DP}}} = \frac{k\sqrt{k}}{\sqrt{2}c_\alpha} \qquad (5)$$

From Eq. (5) it can be concluded that the achievable increase of DRV scales as $k^{3/2}$, in line with what already theorized for analysis based on cross-correlation (Lynch and Scarano, 2013).

The DVR expressions defined in Eq. (3) and Eq. (4) take into consideration the maximum particle displacement and are truly representative for the entire measurement only for a homogeneous flow field (e.g. grid turbulence). In many cases of interest, the velocity and the acceleration vary largely across the field, with the effect that regions at lower velocity are affected by larger relative errors. In this context we define a local principle for the dynamic velocity range:

$$\mathrm{DVR}(x) = \frac{|\mathbf{\Delta X}(x)|}{\sigma_{\Delta \mathrm{X}}} \qquad (6)$$

which represents the inverse of the local relative uncertainty of the velocity (viz. displacement). In order to evaluate the measurement accuracy in the entire domain, the local DVR values defined by Eq. (6) shall be averaged over the entire measurement volume:

$$\overline{\mathrm{DVR}} = \frac{1}{V}\int_V \mathrm{DVR}(x)dV \qquad (7)$$

where V represents the total measurement volume and dV is the sub-volumes in which the DVR is calculated.

A common approach to obtain particle tracks composed of multiple particle positions is the adoption of a time-resolved (TR) image acquisition strategy. The development in terms of illumination and acquisition hardware has permitted the introduction of tracking algorithms capable of following each particle for several time instants. The maximum resolvable velocities are dependent on multiple factors, such as particle density and maximum frequencies of the illuminators and of the cameras. To enable flow measurements at relatively high velocity ($U > 50$ m/s), aside from the double-pulse single-exposure measurements that are always possible, strategies that imply the use of multi-exposed pair of images have been presented and are discussed in the next section.

3. Approaches for multi-exposure PTV

Two different multi-exposure PTV strategies have been presented in literature by Novara et al. (2016) and Sellappan et al. (2020), respectively. Both are based on a two-frame acquisition strategy, with two dual-cavity lasers used to produce four pulses (I-IV), and two exposures in each of the frames. The main difference between the two presented methods lies in the chosen timing strategy, as graphically described in Fig. 2. While Novara et al. (2016) applied a short-long-short timing strategy, with the inter-frame pulse separation time Δt_0 larger than the intra-frame pulse separation time Δt_1, Sellappan et al. (2020) proposed a long-short-long pulse separation time strategy, with $\Delta t_0 < \Delta t_1$. In both cases, the particle position is determined by using the Iterative Particle Reconstruction method (Wieneke, 2013), as implemented in the *Davis* software from LaVision. For both the approaches, the particle pairing is divided into two different steps: the definition of a two-pulse track and then the combination of two two-pulse tracks in a four-pulse track. In the method presented by Novara et al. (2016), two-pulse tracks are created for each of the frames (pairs I-II and III-IV) and linear extrapolation is used to determine the potential middle point of the sequence. Due to the direction ambiguity created by the analysis of two exposure on the same frame, for each two-pulse track, two possible middle points have to be evaluated. When two pairs are matched across the frames, as shown in Fig. 2, the position of the particles is fitted by means of a second-order polynomial regression and the velocity is evaluated at the middle point of the particle track. Sellappan et al. (2020) modified the algorithm by adopting the mentioned long-short-long pulse separation time strategy. In this case, as the first step, a two-pulse track is created across frames, pairing particles at locations II and III. The fact that the two-particle positions are on subsequent frames eliminates the directional ambiguity present in the method from Novara et al. (2016). Furthermore, the increase of the time separation between the two pulses recorded on the same frame leads to an increase in the accuracy of the determination of the velocity and the acceleration along the track (Novara et al., 2019). The two-pulse pair is then extrapolated forward and backwards in time, where the particle positions at instants I and IV are then researched in spherical volume. Once all the four particle positions are determined, a second-order polynomial regression is used to determine the middle point particle position and the correspondent velocity and acceleration.

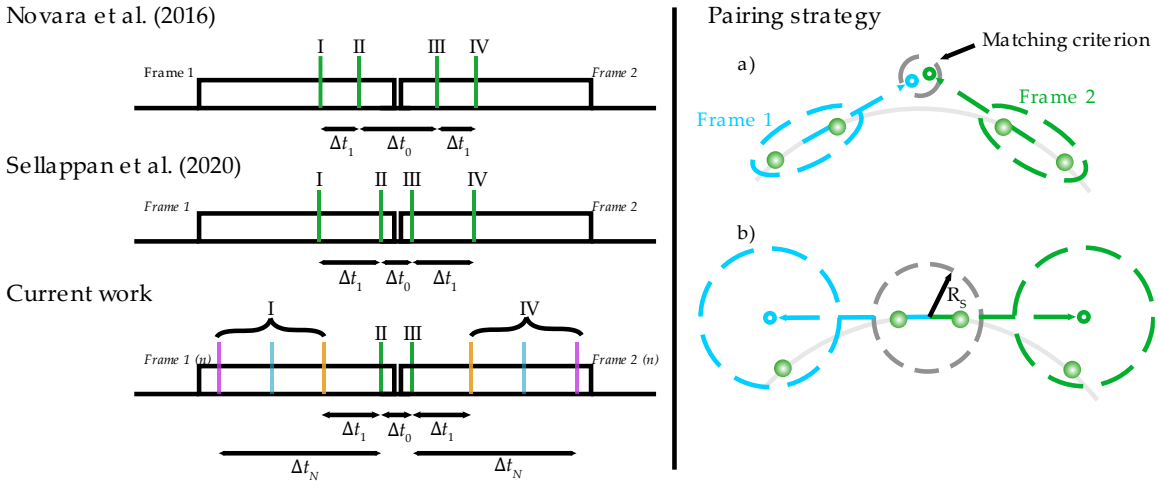

Fig. 2 (Left) Timing strategies of multi-exposure acquisitions presented by Novara et al. (2016), Sellappan et al. (2020) and the current work. Δt_0 represents the inter-frame time separation, while $[\Delta t_1 \ \dots \ \Delta t_N]$ represent the intra-frame pulse separation times. (Right) Schemtatic representation of the different pairing strategies presented by: (a) Novata et al. (2016) and (b) Sellappan et al. (2020).

The choice of Δt_0 and Δt_1 is crucial for both the methodologies since a compromise between accuracy and robustness has to be made. Due to the choice of a single pair of pulse separation times $[\Delta t_0, \Delta t_1]$ for the entire measurement volume, the common strategy is to select the maximum allowed displacement from which, given the expected maximum velocity, a suitable T can be calculated, where $T = \Delta t_0 + 2\Delta t_1$. As previously discussed, this choice creates an inhomogeneity of the measurement accuracy, because low-velocity regions will feature smaller particle image displacements and therefore higher relative uncertainties. Additionally, in these regions, the possibility of particle image overlap arises. Overlapping particle images are a well-known problem since the advent of PIV and several solutions have been presented in the literature (Adrian, 1986; among others). Considering the acquisition strategy proposed by Sellappan et al. (2020), Fig. 3 shows three possible scenarios with decreasing flow velocity. The appearance of one of these scenarios depends on the ratio between the particle displacement $\Delta t|\mathbf{u}|$ and the particle image diameter d_τ.

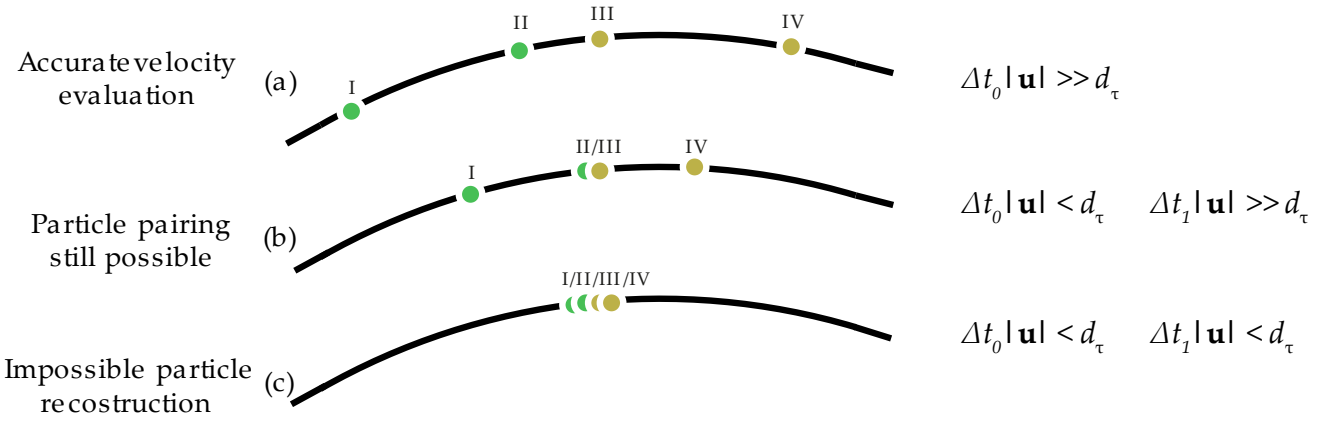

Fig. 3 Example of three possible scenarios obtained by a double-frame double-exposure acquisition strategy at different flow velocities.

Scenario (a) describes the desired situation to obtain both an accurate particle position and velocity determination and is achieved when $\Delta t_0 \, |\mathbf{u}| \gg d_\tau$, with $\Delta t_1 > \Delta t_0$. The pulse separation times Δt_0 and Δt_1, however, cannot be extended indefinitely, due to the appearance of false pairing (Saredi et al., 2020) and truncation errors (Boillot and Prasad, 1996). Considering scenario (b), even if the particle images corresponding to the pulses II and III overlap, this does not prevent the particle pairing since they are located on different frames. However, the small displacement between the particle positions II and III causes is a low accuracy of the velocity vector used to predict the particle positions at I and IV, increasing the probability of false pairings. Scenario (c) describes instead the situation when all four particle images overlap. In this case, particle position determination within each frame is not possible anymore. For this reason, it becomes clear that it is desirable to obtain the scenario (a) in the entire measured volume. This is not achievable with a single combination of Δt_0 and Δt_1.

4. The adaptive multi-step multi-exposure PTV algorithm

Recalling the definition of Eq. (6) we propose a method that homogenizes the relative error by producing a rather constant local particle displacement $|\mathbf{\Delta X}|$. This principle directly mimics the concept anticipated by Hain and Kähler (2007, multiframe particle image velocimetry) but in the context of Lagrangian particle tracking with multi-exposed images. The main ingredients of this technique are the availability of a predictor, in terms of time-average velocity $\overline{\mathbf{V}}_{\mathrm{pred}}$ and fluctuations root-mean-square $\mathbf{u}'_{\mathrm{pred}}$, and a strategy to vary the pulse separation time pairs [Δt_0 Δt_1] across the measurement campaing. To obtain the former, a multi-step approach is considered, similar to the one presented by Saredi et al. (2020). First, a double-frame single-exposure acquisition is performed and processed to produce a first estimation of the velocity field. The

Lagrangian information obtained from the analysis of the double-frame single-exposure images is mapped onto a uniform Eulerian grid following the ensemble averaging procedure presented by Agüera et al. (2016), thus yielding the velocity predictor $\overline{\mathbf{V}}_{\mathrm{pred}}$. The analysis of the velocity predictor in the measurement volume allows the determination of the time interval boundaries (T_{min}, T_{max}) for the successive multi-exposure image acquisition, based on the ratio between the desired displacement $|\mathbf{\Delta X}|_0$ and the local flow velocity.

The procedure implemented to determine the suitable pulses separations is as follows. The distribution of the absolute velocity obtained by the analysis of the predictor velocity field is divided into N intervals, ranging between 0 and $|\overline{\mathbf{V}}|_{\max}$ with a decreasing reference velocity V_n is assigned to the n$^{\mathrm{th}}$ interval. The definition of the desired displacement allows to evaluate the required total time T for each interval through the equation:

$$T_n = \frac{|\mathbf{\Delta X}|_0}{V_n} = \Delta t_0 + 2\Delta t_1 \qquad (8)$$

Once the total time for each interval is set, N acquisitions are performed with the pair $[\Delta t_0, \Delta t_1]_n$ varying accordingly to respect the indications given by Eq. (8). To select which tracks have to be considered for each measurement, a spatial map is created starting from the Eulerian grid on which $\overline{\mathbf{V}}_{\mathrm{pred}}$ was mapped. A value of T_n is assigned to each sub-volume of the Eulerian grid and only the tracks that come from the corresponding acquisition are then considered. Finally, the same *binning* procedure (Agüera et al., 2016) is applied to obtain the final time-average velocity field.

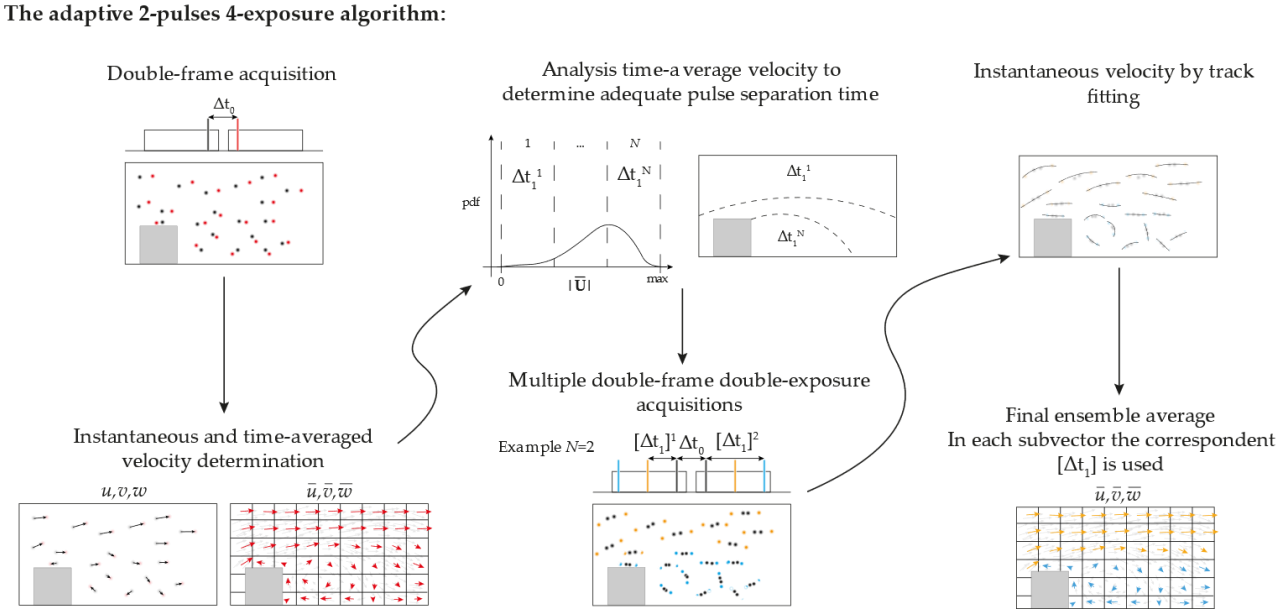

Fig. 4 Schematic representation of the flowchart of the proposed methodology.

In summary, the proposed methodology is schematically represented in the flowchart presented in Fig. 4.

5. Experimental assessment

An experiment is conducted in the Aerodynamics Laboratory of TU Delft to assess the effectiveness of the proposed methodology. The near-wake of a 10 cm diameter truncated cylinder, characterized by a height/diameter ratio of 1, is investigated in a low-speed wind tunnel (W-Tunnel) equipped with an open test section of 60×60 cm^2 . The free-stream velocity is set to 5 m/s, which implies a Reynolds number based on the cylinder diameter D equal to 3.3×10^4. The cylinder is positioned in the mid-span of a flat plate, equipped with a tripping device past the leading edge to force laminar to turbulent boundary layer transition. The shape of the plate leading edge is cubic super-elliptical of axis ratio 6 to minimize flow separation occurrence (Narashima and Prasad, 1994).

A measurement volume of $25 \times 20 \times 20$ cm^3 captures the near-wake of the truncated cylinder. The measurement setup is shown in Fig. 5. The flow is seeded with helium-filled-soap-bubbles (HFSB), generated by a 50×100 cm^2 seeding rake positioned in the settling chamber of the wind tunnel. The generator contains 200 bubble-producing nozzles, which nominally produce 30,000 bubbles per second each (Faleiros et al., 2019). In order to control the mass flow of soap, air and helium, a homemade fluid supply unit (FSU) is used. Two LaVision LED-Flashlight 300 illumination units positioned above the cylinder illuminate the measurement region, imaged by four Photron Fast CAM SA1 cameras (CMOS, 1024 × 1024 pixels, 12 bits). Three of the cameras are equipped with 50 mm objectives, while one (the closest to the cylinder) is equipped with a 35 mm objective.

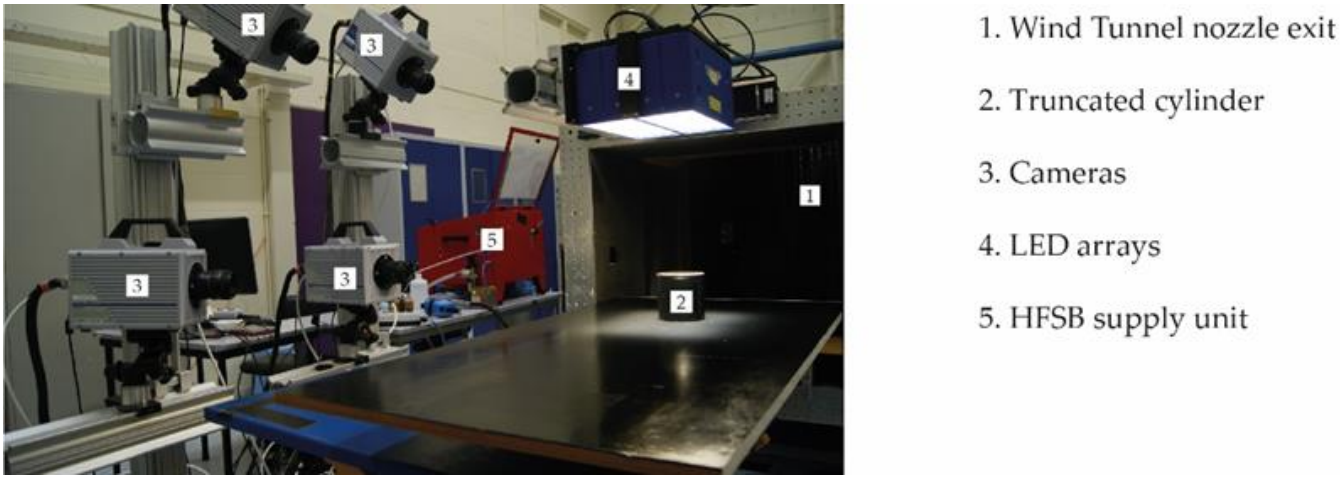

Fig. 5 Picture of the experimental setup used to study the near wake of a square cylinder. The measurement volume of $25 \times 20 \times 20$ cm^3 corresponds to the illuminated region.

To evaluate the performances of a new algorithm it is common to use synthetic datasets for which a reference is available and the comparison between the results of each technique is easily comparable. Several examples of this strategy are presented in the literature (Sciacchitano et al., 2012; Novara and Scarano, 2013; amongst others). One conclusion from these works is that replicating the measurement error in a synthetic dataset is far from being straightforward. For this reason, for this study, a full experimental assessment has been performed. The needed reference has been created by sampling the flow with a relatively high frequency at 5 kHz ($\Delta t = 0.2$ ms) to create relative long tracks (more than 20 expositions). The acquired images (2 datasets of 7000 images each) have been then processed with the PTV algorithm STB. For each of the reconstructed particle tracks, particle positions have been fitted with a least-square regression, as discussed by Schanz et al. (2016). The tracks obtained from the two acquisitions have been then combined, obtaining $5x10^5$ tracks in total, which are considered as reference for the application of the other approaches.

To apply both the standard double-frame PTV, the 4-pulses approach by Sellappan et al. (2020), hereafter referred as static 4P-2F, and the method proposed in this study, referred as adaptive 4P-2F, double-frame datasets are needed. In order to be able to quantitatively evaluate the performances of the different approaches, the particle reconstruction in a 3D space, usually performed by IPR, has been substituted with direct input from the tracks computed by STB. For each of the tracks, the raw particle positions at the select time instants are considered, as schematically shown in Fig. 6, and used to evaluate the velocity according to each of the analyzed methods.

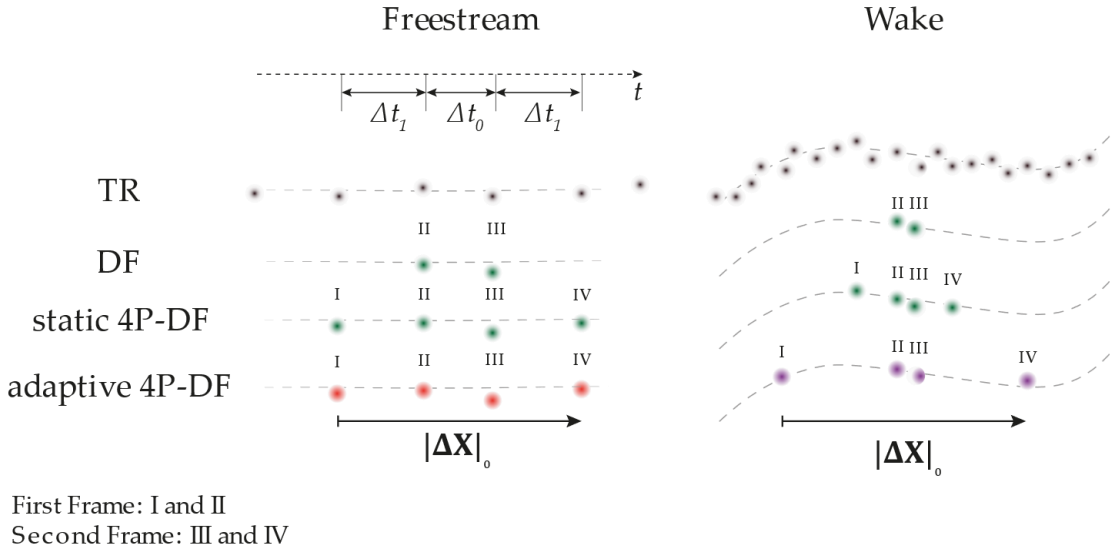

Fig. 6 Schematic representation of the mechanism behind the particle selection to generate the multi-frame datasets from the STB tracks. The difference between the static and the adaptive 4P-DF emerges in the region of low velocity, where the intra-frame pulse separation time Δt_1 is increased to obtain a constant particle displacement $|\mathbf{\Delta X}|_0$.

The main difference between the static and the adaptive 4P-2F methods is visualized in Fig. 6. While in the region characterized by a high particle displacement, such as the freestream, the two methods adopt the same pair of pulse separation times $[\Delta t_0, \Delta t_1]$, the inter-frame pulse separation time Δt_1 is increased for the adaptive 4P-2F where the displacement decreases, such as in the recirculation or separation regions. The results obtained by applying the different timing schemes are presented in the next section.

5. Results

Applying STB to all the acquired time-resolved images, a total of 550000 tracks were obtained. A subsample of them is presented in Fig. 7 (left), where the lines are coloured based on the particle velocity. Fig. 7 (right) shows the velocity field along the centre plane obtained by ensemble averaging the Lagrangian particle velocities in subvolumes of $3 \times 3 \times 3$ cm^3 with an overlap of 75%, producing a final grid with a vector pitch of 7.5 mm.

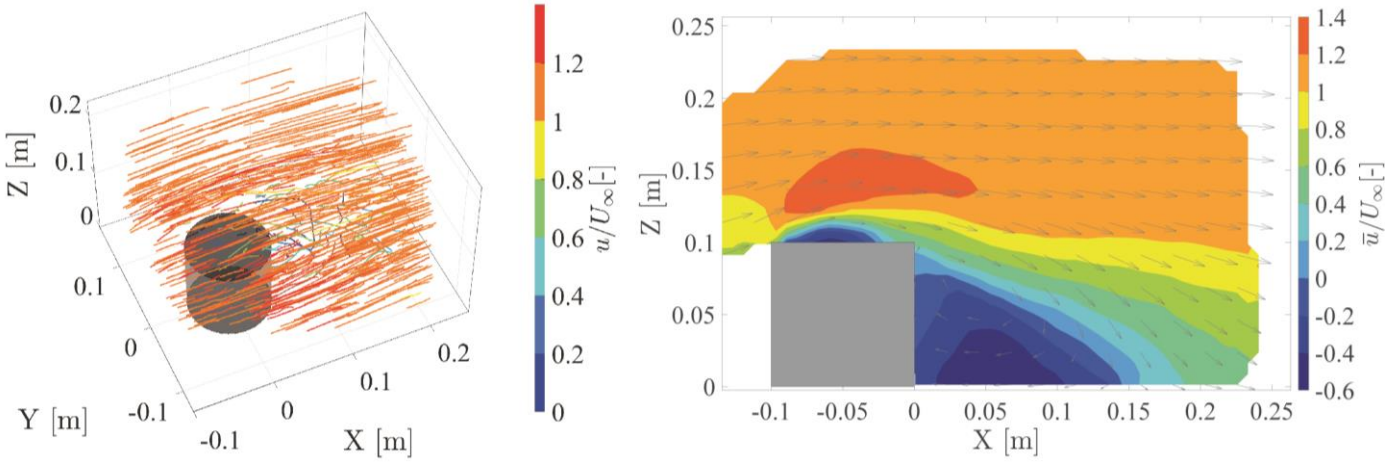

Fig. 7 (left) Snapshot of a subset of the instantaneous Lagrangian particle tracks coloured by their normalized streamwise velocity. (Right) Representation of the time-average velocity field $\bar{u}$ normalized by the freestream velocity U_∞ along the plane $Y = 0$ mm.

The flow in the back of the cylinder shows the characteristics of the near wake of a bluff body. A region of reverse flow is visible on the top surface of the cylinder, with the flow separating at the leading edge. Above the separation region, accelerated flow is measured. This is due to the streamline curvature due to the flow separation on the top surface. The near-wake of the cylinder is characterized by the presence of a recirculation region that extends until $\frac{X}{D} = 1.5$.

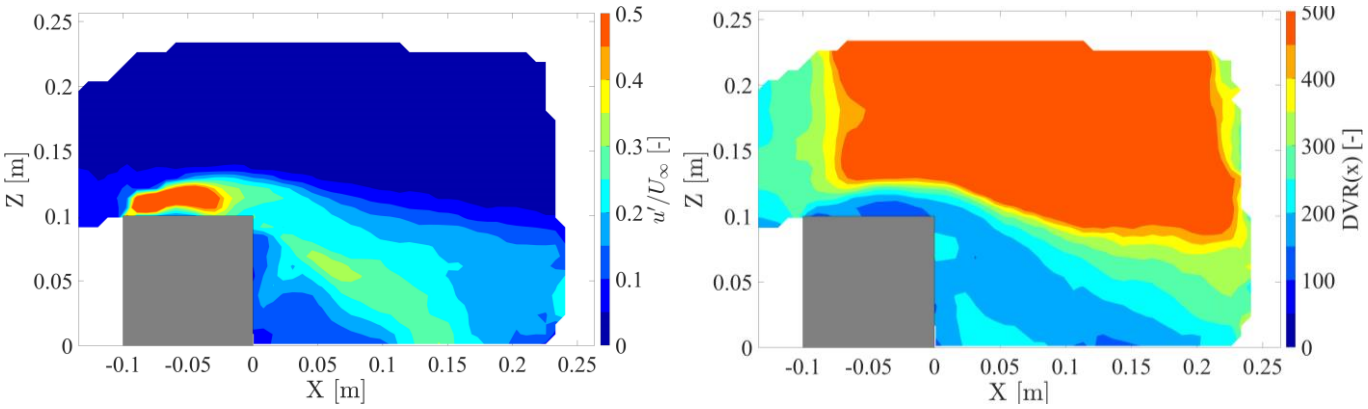

Fig. 8 (Left) Contour of the root-mean-square of the normalized streamwise velocity fluctuations u'/U_∞ given by STB at $Y = 0$ mm. (Right) Contour of the averaged relative uncertainty on the velocity determination.

Fig. 8 (left) presents the fluctuating component of the streamwise velocity obtained by STB. It is noticeable the effect of the shear layer caused by the separation at the leading edge of the top surface of the cylinder, where the fluctuating component overcomes 50% of the freestream velocity. Moving downstream, the shear region diffuses and increases its size while decreasing the level of fluctuations to 35% at the centre of the recirculation region. Fig. 8 (right) illustrates the spatial distribution of the local DVR evaluated by Eq. (6). In order to determine the relative uncertainty of the velocity, the relative uncertainty of the particle position ϵ_x is needed. To evaluate the latter, the average of the discrepancy between the raw and the fitted particle position is used, following the equation:

$$\epsilon_x = \frac{1}{k}\sum_{i=1}^{k} |\mathbf{X}_{\mathrm{i,raw}} - \mathbf{X}_{\mathrm{i,fit}}| \qquad (9)$$

The value of DVR depends on the local particle displacement and varies between O(10^3) in the freestream region, where the displacement is maximum, to O(10^2) in the separation region above the top surface of the cylinder. The low uncertainty of the velocity determination allows to use the STB particle tracks as reference for the evaluation of the three mentioned techniques: double-frame single exposure (DF), 4-pulse double-frame with fixed time separation (static 4P-2F) and the proposed adaptive algorithm based on 4-pulse double-frame with variable time separation recordings (adaptive 4P-2F). The first method analyzed is the double-frame single exposure (DF), with a pulse separation time $\Delta t_0 = 2\Delta t_{STB}$.

In order to evaluate the precision of the measurement, two different parameters are here calculated: the local DVR evaluated following Eq. (6) and the local difference between the reference and the calculated field, evaluated as:

$$\Delta = |u_{DF} - u_{STB}| \qquad (10)$$

which is calculated for each track. To evaluate the spatial variation of Δ, its value is spatially averaged through the same ensemble process described for the velocity.

Fig. 9 (left) shows the spatial distribution at $Y = 0$ mm of the local DVR evaluated as prescribed by Eq. (6). Its value varies drastically within the measurement volume, reaching its maximum in the freestream region (DVR~20). In the near wake, more specifically in the recirculation region, Its value drops below 4 due to the small particle displacement. The same region is characterized by the highest deviation between the instantaneous velocity measured by STB and DF, in average ~8%, as shown in Fig. 9 (right).

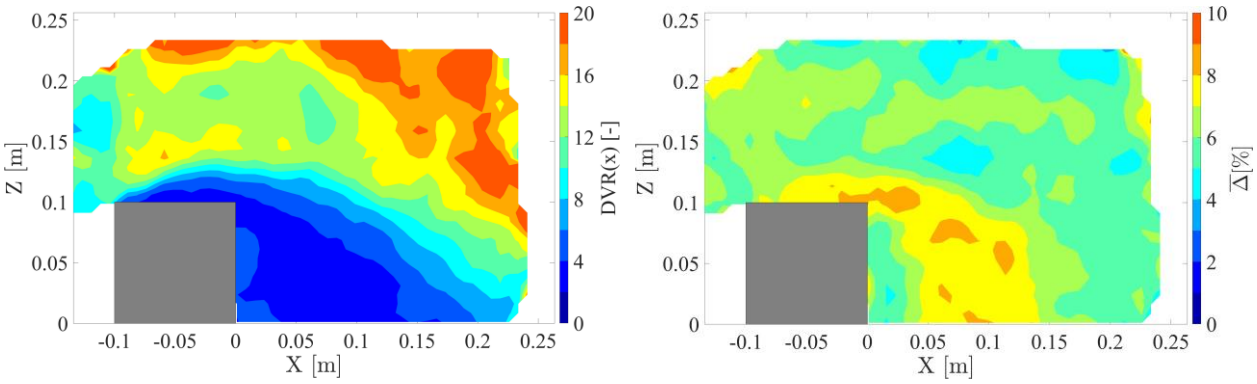

Fig. 9 (Left) Contour of the local DVR obtained by DF at $Y = 0$ mm. (Right) Contour of the mean deviation $\bar{\Delta}$ between DF result and the reference, as a percentage of the freestream velocity.

To evaluate the performance of the static 4P-2F method, the following timing strategy is selected: $\Delta t_0 = \Delta t_{STB}$ and $\Delta t_1 = 3\Delta t_{STB}$. Once the four particles are selected from each of the STB tracks, a second-order polynomial fit is evaluated through the raw positions of the selected particles. The adoption of a multi-exposure strategy leads to an increase of the obtainable local DVR, as shown in Fig. 10 (left). As for the DF method, the peak of DVR is reached in the freestream region above the cylinder. In this region, the increase of particle displacement doubles the obtainable DVR, reflecting the 100% increase of T. The effect of the time extension can be detected also in the recirculation region, where the obtainable DVR doubles as well, from ~5 to ~10. Fig 10 (right) present the average deviation between the velocity calculated by STB and by the static 4P-2F method. A general reduction of 2-3% is obtained in the entire field when compared to the DF method.

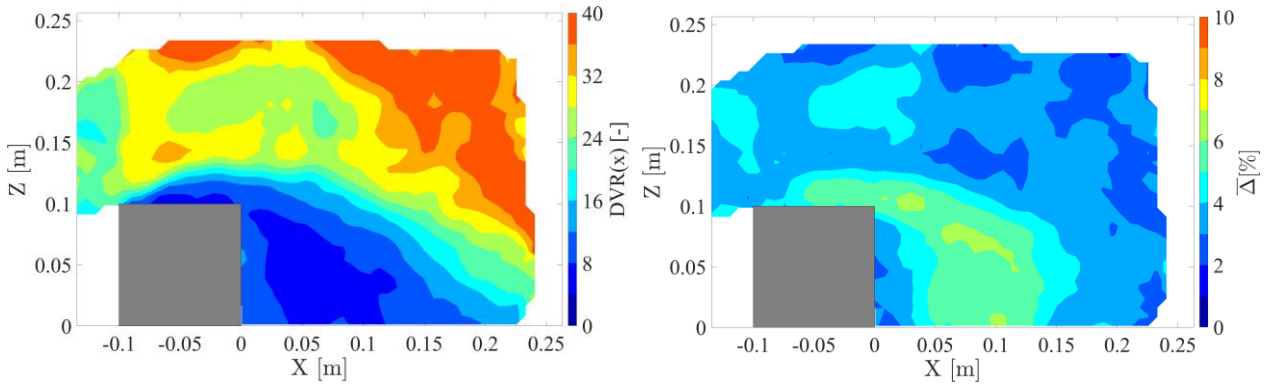

Fig. 10 (Left) Contour of the local DVR obtained by static 4P-2F at $Y = 0$ mm. (Right) Contour of the mean deviation $\bar{\Delta}$ between static 4P-2F result and the reference, as a percentage of the freestream velocity.

In order to determine the pairs $[\Delta t_0, \Delta t_1]_n$ to be used for the adaptive 4P-2F method, the pdf of the distribution of absolute velocities of the predictor field (DF field in this case) has to be evaluated and is shown in Fig. 11 (left). The entire range of velocities is equally divided in N subgroups and for each of them a reference velocity V_n at the middle of the subrange is selected. The correspondent T_n is then evaluated using Eq. (8). It is decided to set $N = 3$ so as to consider three pairs of $[\Delta t_0, \Delta t_1]_n$. Table 1 shows the pulse separation times selected in the three regions of different velocities.

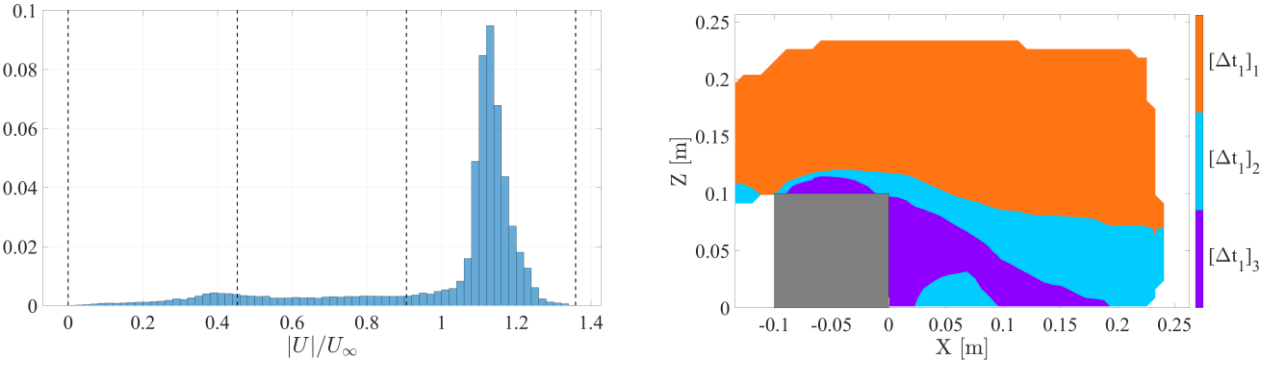

Fig. 11 (Left) Distribution of the normalized absolute velocity |**U**| obtained by analysing the reference velocity field. (Right) Illustration of the spatial distribution of the time extension applied by the proposed methodology.

Table 1: Distribution of pulse separation time pair given the local velocity.

Region #	Local flow velocity	Δt_0	Δt_1	T_n
1	$\|\boldsymbol{U}\|/U_\infty > 0.9$	Δt_{STB}	2 Δt_{STB}	5 Δt_{STB}
2	$0.45 < \|\mathbf{U}\|/U_\infty < 0.90$	Δt_{STB}	4 Δt_{STB}	9 Δt_{STB}
3	$\|\boldsymbol{U}\|/U_\infty < 0.45$	Δt_{STB}	8 Δt_{STB}	17 Δt_{STB}

Following the indication given in Table 1, Fig. 11 (right) shows the regions where the different pulse separation time pairs are used. While in the freestream the time strategy is equal to the one used for the static 4P-2F method, the total time is stretched up to three times in the recirculation region to increase the particle displacement and in turn the DVR.

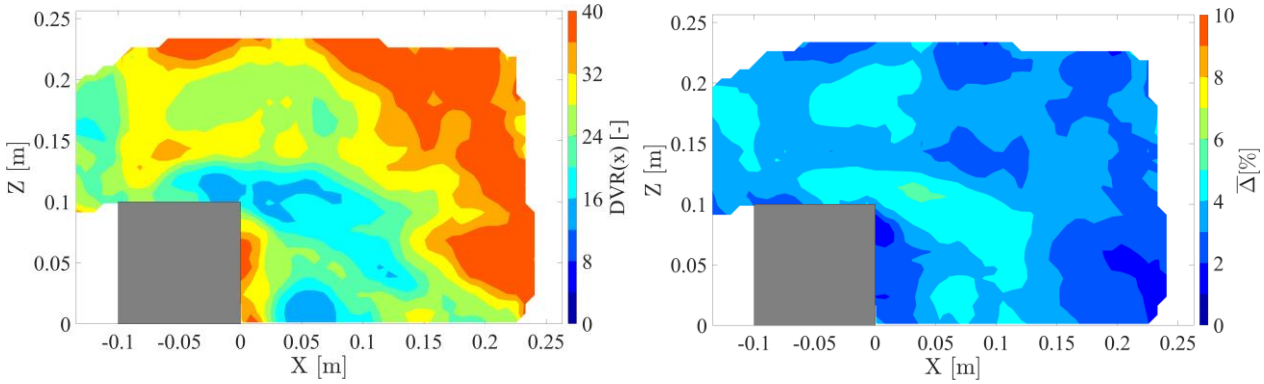

Fig. 12 Contour of the local DVR obtained by the adaptive 4P-2F at $Y = 0$ mm. (Right) Contour of the mean deviation $\overline{\Delta}$ between the adaptive 4P-2F and the reference, as a percentage of the freestream velocity.

The increase in total displacement improves the precision of the velocity determination, as illustrated by the distribution of the local DVR shown in Fig. 12 (left). When compared to the DF strategy, the local DVR in the recirculation region increases of ~150% while, compared to the static 4P-2F method, an increase of ~50% is obtained. The increase in precision is detectable also when the deviation from the reference $\overline{\Delta}$ is evaluated, as shown in Fig. 12 (right). The increment of the total displacement allows for an increase in the precision of the particle fit and reduces the discrepancy from the reference velocity, quantifiable in 28% in the wake region where the time stretching reaches the maximum.

6. Conclusions

In this paper, a new adaptive acquisition strategy has been presented. The method is based on a multi-step approach. Firstly, a double-frame single-exposure acquisition is analyzed and Reynolds decomposition is applied to the calculated velocity field to obtain the time-averaged velocity field $\overline{\mathbf{u}}$. The use of a double-frame single-exposure strategy allows to evaluate the velocity field in a robust but low precise manner. The predicted velocity field is used then to obtain a series of pulse separation times for the successive acquisition of a series of double-frame double-exposure datasets. The time separation pairs are selected in order to obtain a rather constant particle displacement across the measurement volume. Finally, the tracks computed analysing the different acquisitions are merged to produce the final description of the flow field. The proposed methodology has been tested considering the near-wake of a truncated cylinder. To quantitatively

evaluate the performance of the mentioned algorithms, a reference has been constructed with the Lagrangian Particle tracking algorithm shake-the-box applied to a highly sampled dataset. The results show the benefit obtained by the increment of particle displacement in the region characterized by low velocities in terms of measurement precision. Further studies on the effect of particle concentration and truncation errors will be carried out in the future.

References

Adrian, R. J. (1986). Image shifting technique to resolve directional ambiguity in double-pulsed velocimetry. Applied Optics 25:21.

Adrian, R. J. (1997). Dynamic ranges of velocity and spatial resolution of particle image velocimetry. Measurement Science and Technology, 8, 1393–8.

Adrian, R. J., & Westerweel, J. (2011). *Particle Image Velocimetry*. Cambridge University Press.

Agüera, N., Cafiero, G., Astarita, T., & Discetti, S. (2016). Ensemble 3D PTV for high resolution turbulent statistics. Measurement Science and Technology, 27(12), 124011.

Boillot, A., & Prasad, A. K. (1996). Optimization procedure for pulse separation in cross-correlation PIV. Experiments in Fluids, 21, 87-93.

Cierpka, C., Lütke, B., & Kähler, C. J. (2013). Higher order multi-frame particle tracking velocimetry. Experiments in Fluids , 54 (5), 1-12.

Faleiros, D.E., Tuinstra, M., Sciacchitano, A., & Scarano, F. (2019). Generation and control of helium-filled soap bubbles for PIV. Exp. Fluids 60:17.

Hain, R., & Kähler, C. J. (2007). Fundamentals of multiframe particle image velocimetry (PIV). Experiments in fluids, 42(4), 575-587.

Kähler, C. J., Astarita, T., Vlachos, P. P., Sakakibara, J., Hain, R., Discetti, S., La Foy, R., & Cierpka, C. (2016). Main results of the 4th International PIV Challenge. Experiments in Fluids57:97.

Lynch, K., & Scarano, F. (2013). A high-order time-accurate interrogation method for time-resolved PIV. Measurement Science and Technology, 24, 035305.

Narasimha, R., & Prasad, S. N. (1994). Leading edge shape for flat plate boundary layer studies. Experiments in Fluids, 17(5), 358-360.

Novara, M., & Scarano, F. (2013). A particle-tracking approach for accurate material derivative measurements with tomographic PIV. Experiments in fluids, 54(8), 1-12.

Novara, M., Schanz, D., Reuther, N., Kähler, C. J., & Schröder, A. (2016). Lagrangian 3D particle tracking in high-speed flows: Shake-The- Box for multi-pulse systems. Experiments in Fluids, 57(8), 128.

Novara, M., Schanz, D., Geisler, R., Gesemann, S., Voss, C., & Schröder, A. (2019). Multi-exposed recordings for 3D Lagrangian particle tracking with Multi-Pulse Shake-The-Box. Experiments in Fluids, 60(3), 44.

Saredi, E., Sciacchitano, A., & Scarano, F. (2020). Multi-Δt 3D-PTV based on Reynolds decomposition. Measurement Science and Technology, 31, 084005.

Scarano, F. (2012) Tomographic PIV: principles and practice. Measurement Science and Technology, 24(01), 1-28.

Schanz, D., Gesemann, S., & Schröder, A. (2016). Shake-The-Box: Lagrangian particle tracking at high particle image densities. Exp Fluids 57, 70.

Schneiders, J. F., Scarano, F., Jux, C., & Sciacchitano, A. (2018). Coaxial volumetric velocimetry. Measurement Science and Technology, 29(6), 065201.

Schneiders, J. F., Scarano, F., Jux, C., & Sciacchitano, A. (2018). Coaxial volumetric velocimetry. Measurement Science and Technology, 29(6), 065201.

Sciacchitano, A., Scarano, F., & Wieneke, B. (2012). Multi-frame pyramid correlation for time-resolved PIV. Experiments in fluids, 53(4), 1087-1105.

Sellappan, P., Alvi, F. S., & Cattafesta, L. N. (2020). Lagrangian and Eulerian measurements in high-speed jets using Multi-Pulse Shake-The-Box and fine scale reconstruction (VIC#). Experiments in Fluids, 61, 157.

van Oudheusden, B. (2013). PIV-based pressure measurement. Measurement Science and Technology, 24, 032001.

Wieneke, B. (2012). Iterative reconstruction of volumetric particle distribution. Measurement Science and Technology, 24(2), 024008.